Chemical Science

ROYAL SOCIETY OF CHEMISTRY

EDGE ARTICLE

View Article Online
View Journal | View Issue

Cite this: *Chem. Sci.*, 2026, **17**, 1186

All publication charges for this article have been paid for by the Royal Society of Chemistry

Received 10th September 2025
Accepted 13th November 2025

DOI: 10.1039/d5sc06967j

rsc.li/chemical-science

Breaking the lithium deposition limit: *in situ* fabrication of a CoN-doped carbon skeleton membrane for anode-free lithium metal batteries

Wenyu Ma,[a] Haiyang Wu,[a] Lingtong Zhu,[a] Zhenming Xu, *[a] Bing Ding, [ab] Hui Dou *[ab] and Xiaogang Zhang *[ab]

Anode-free lithium metal batteries (AFLMBs) leverage a bare current collector (CC) as a lithium deposition substrate to achieve high energy density and reduced manufacturing costs. However, severe nucleation overpotential and dendritic growth, rooted in the Cu–Li lattice mismatch, hinder their practical deployment. Herein, a dense zeolitic imidazolate framework-67 (ZIF-67) polycrystalline membrane is epitaxially grown *in situ* on Cu CC *via* liquid-phase epitaxy and subsequently converted into a CoN-doped carbon skeleton membrane (67 MC@Cu) through thermal treatment. The embedded CoN nanoparticles, evolved from {CoN_4} units in ZIF-67, serve as highly lithiophilic sites that dynamically regulate lithium nucleation and suppress dendrite formation. The binder-free fabrication maximizes the exposure of active sites while preserving the functionality of the MOF-derived architecture. As a result, full cells assembled with 67 MC@Cu exhibit markedly enhanced cycling stability, retaining 92.0% capacity after 280 cycles—far surpassing 20.2% retention of commercial carbon-coated Cu (C@Cu). This work provides an effective interfacial engineering strategy to advance the practical implementation of AFLMBs.

1. Instruction

High energy density remains a primary objective for electrochemical energy storage technologies to meet the evolving global energy demands and growing application requirements.[1–3] Lithium metal batteries (LMBs) have attracted extensive attention owing to their exceptional theoretical capacity (3860 mA h g^{-1}) and low electrochemical potential (−3.04 V *vs.* the standard hydrogen electrode). However, their practical application is hindered by the low coulombic efficiency (CE), undesirable side reactions, and formation of lithium dendrites.[4–7] Furthermore, the excessive lithium content in commercial Li foil (50–400 μm thick) reduces energy density and increases safety risks in LMBs.[8–10]

Anode-free lithium metal batteries (AFLMBs), which utilize a bare current collector (CC) as the Li^+ deposition substrate (Fig. 1a), offer the potential for high energy density at low manufacturing costs.[11–13] Nevertheless, the unstable Li/CC interface and the absence of active materials severely limit their cycle life and thus their practical viability. These issues, largely originating from the lattice mismatch between metallic Li and Cu CC, have prompted efforts to modify the structure and surface properties of Cu CCs.[14–16] Such strategies aim to enhance the reversibility of Li deposition/stripping and extend the cycling stability of AFLMBs. Carbon-modified CCs, particularly commercial carbon-coated Cu (C@Cu) foil, have been extensively utilized in lithium-ion batteries (LIBs).[17–20] Recently, De Volder *et al.* fabricated a three-dimensional porous composite CC by electrodepositing carbon nanotubes onto Cu, which enhanced the mechanical elasticity of Cu foam and reduced cell resistance.[21] However, precise regulation of Li deposition using a single carbon-based material remains challenging due to limited functionality and insufficient material diversity. To address this, Zhu *et al.* developed a Se-decorated carbon cloth host, and the highly lithiophilic nano-Se imparted excellent Li wettability.[22] Therefore, further improvements in Li deposition layer quality can be achieved by simultaneously introducing highly lithiophilic metal nanoparticles and highly conductive carbon materials onto Cu CCs.[23,24]

Metal–organic frameworks (MOFs), a class of porous crystalline materials composed of metal ions/clusters coordinated with organic ligands, offer an ideal platform for such modifications. Upon thermal treatment, the organic ligands are converted into a conductive carbon skeleton, while the metal nodes transform into uniformly dispersed metal-based nanoparticles. This property has made MOFs attractive as sacrificial templates for fabricating metal nanoparticle-doped carbon materials.[25–28] Compared with the carbon layer of C@Cu, MOF-derived carbon

[a]*Jiangsu Key Laboratory of Materials and Technologies for Energy Storage, College of Materials Science and Technology, Nanjing University of Aeronautics and Astronautics, Nanjing 211106, China. E-mail: xuzhenming@nuaa.edu.cn; dh_msc@nuaa.edu.cn; azhangxg@nuaa.edu.cn*

[b]*National Key Laboratory of Mechanics and Control for Aerospace Structures, Institute for Frontier Science, Nanjing University of Aeronautics and Astronautics, Nanjing 210016, P.R. China*

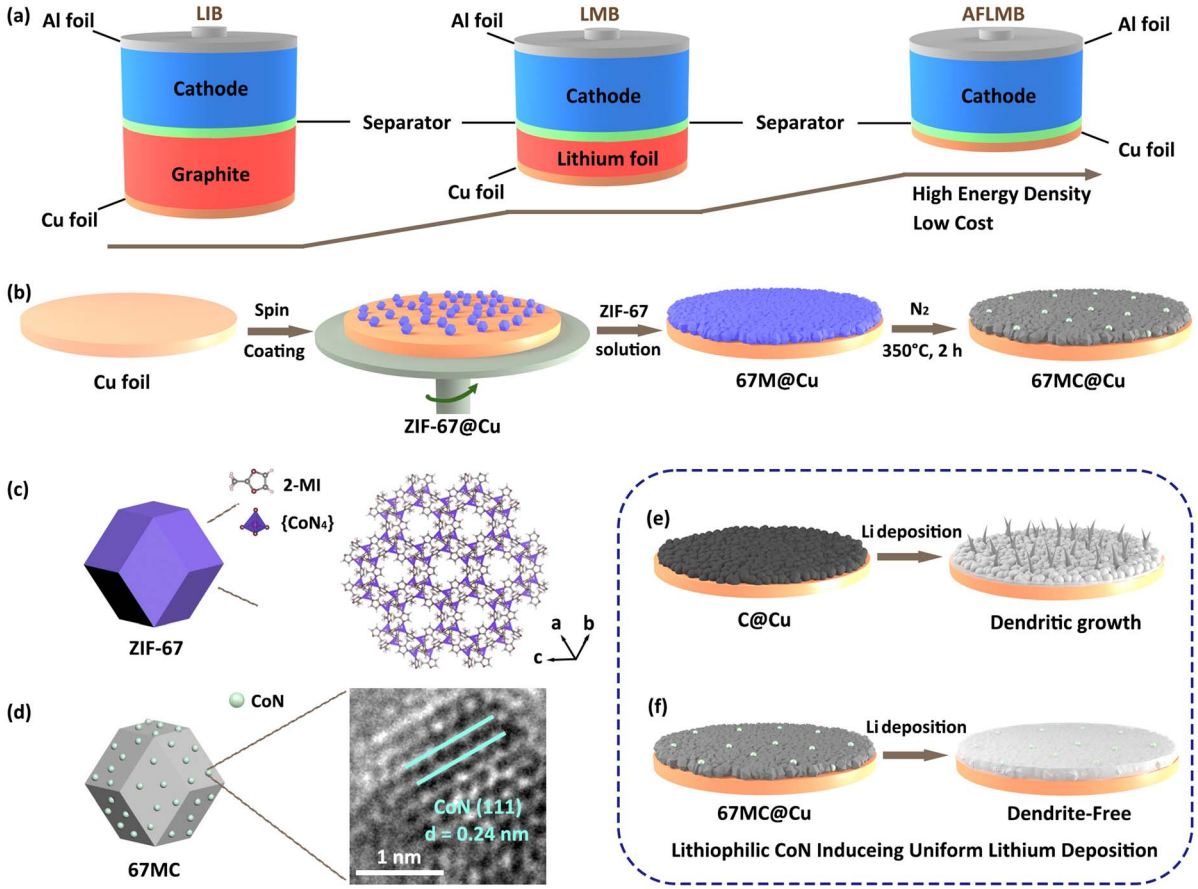

Fig. 1 (a) Schematic illustration of the structures of LIBs, LMBs, and AFLMBs. (b) The preparation process of 67 MC@Cu. (c) The structure and ball-and-stick model of ZIF-67. (d) The structural model and HRTEM image of 67 MC. Schematic illustration of Li^+ deposition on the commercial (e) C@Cu CC and (f) 67 MC@Cu CC.

skeleton contains homogeneously distributed metal nanoparticles that serve as abundant lithiophilic sites to guide Li^+ nucleation. However, most reported MOF-derived carbon coatings still rely on polymeric binders such as polyvinylidene fluoride (PVDF) or polytetrafluoroethylene (PTFE) to attach the powders onto Cu CC. The use of such binders often results in weak interfacial adhesion, non-uniform and discontinuous distribution of lithiophilic sites, and reduced electronic conductivity. Moreover, the insulating binder can block active sites, thereby significantly compromising the overall effectiveness of the surface modification.[29–33]

To overcome these limitations, this work employs a liquid-phase epitaxial growth strategy to *in situ* fabricate a dense and continuous zeolitic imidazolate framework-67 (ZIF-67) polycrystalline membrane (67M) directly on Cu CC (Fig. 1b). Subsequent thermal treatment transformed the 67M layer into a CoN-doped carbon skeleton membrane (67 MC@Cu), enabling complete, binder-free surface modification of the Cu CC and generating abundant, uniformly distributed lithiophilic CoN sites (Fig. 1c and d). The resulting 67 MC membrane effectively directs uniform Li^+ deposition, suppresses dendrite growth, and improves the integrity of the Li deposition layer (Fig. 1e and f). As an anode for AFLMBs, 67 MC@Cu exhibits superior cycling stability and practical applicability compared to commercial C@Cu foil.

2. Results and discussion

The fabrication process of 67 MC@Cu is illustrated in Fig. 1b. Initially, ZIF-67 powders were evenly seeded onto Cu foil (ZIF-67@Cu) *via* a spin-coating technique. ZIF-67@Cu was then immersed in a ZIF-67 growth solution, where the crystal seeds guided the epitaxial growth of ZIF-67, resulting in the formation of a continuous and dense ZIF-67 polycrystalline membrane on the Cu foil (67M@Cu). Subsequent thermal treatment in an N_2 atmosphere converted 67M@Cu into a CoN-doped carbon skeleton membrane (67 MC@Cu). According to the immersion time and thermal treatment temperature, the obtained samples were designated as Cu-2h-400 (2 h growth followed by thermal treatment at 400 °C) and Cu-3h-350 (3 h growth followed by thermal treatment at 350 °C).

The morphological evolution of the Cu foil surface during the fabrication of 67 MC@Cu was examined by scanning electron microscopy (SEM) (Fig. 2a). Spin-coated ZIF-67 particles serve as nucleation seeds (Fig. 2b), enabling rapid membrane formation. After 1 h of immersion in the growth solution, the Cu foil surface is largely covered by the ZIF-67 membrane

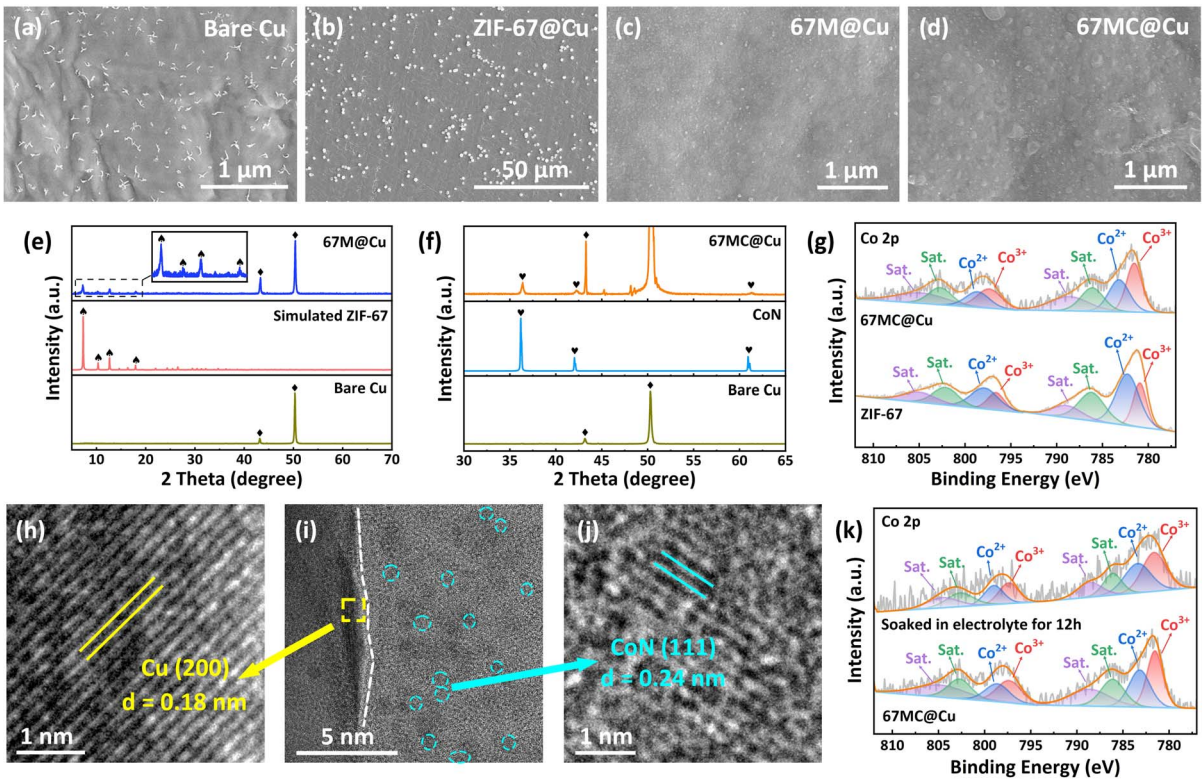

Fig. 2 SEM images of (a) bare Cu, (b) ZIF-67@Cu, (c) 67M@Cu, and (d) 67 MC@Cu. (e) XRD patterns of bare Cu, simulated ZIF-67, and 67M@Cu. (f) XRD patterns of bare Cu, CoN, and 67 MC@Cu. (g) High-resolution Co 2p XPS spectra of ZIF-67 and 67 MC@Cu. (h–j) TEM images of 67 MC@Cu. (k) High-resolution Co 2p XPS spectra of 67 MC@Cu, both pristine and after immersion in electrolyte for 12 h.

(Fig. S1). Extending the growth time to 2 h results in the formation of a complete and well-intergrown ZIF-67 crystal membrane on the Cu foil (Fig. 2c). Following thermal treatment, SEM analysis confirms the transformation of 67M@Cu into 67 MC@Cu (Fig. 2d). Cross-sectional SEM further reveals a tight interfacial contact between 67 MC and Cu foil, with a uniform membrane thickness of 3.4 μm (Fig. S2). X-ray energy dispersive spectroscopy (EDS) verifies the homogeneous distribution of C, N, and Co elements in 67 MC@Cu, demonstrating the structural integrity of the 67 MC membrane (Fig. S3). Complementary atomic force microscopy (AFM) shows that the height variation on the 67 MC@Cu surface (566 nm) is smaller than that on bare Cu foil (677 nm), indicating that the 67 MC membrane promotes planarization of the CC (Fig. S4). Moreover, optical observation reveals that, due to light reflection from the dense 67 MC membrane, 67 MC@Cu exhibits a visible color gradient under natural light (Fig. S5).[34–36] SEM images of Cu-2h-400 and Cu-3h-350 further confirm that although the surface morphology evolves with higher thermal temperature and membrane thickness increases with longer immersion times, the modified membrane layer remains continuous and dense (Fig. S6).

To examine the structural evolution, different CCs were systematically characterized using X-ray diffraction (XRD) (Fig. 2e). The XRD pattern of 67M@Cu exhibits well-defined diffraction peaks in the low-angle region corresponding to the (011), (002), (112), and (222) planes of ZIF-67. In the XRD pattern of 67 MC@Cu, the diffraction peaks at $2\theta = 36°$ and 42° are attributed to CoN formation after thermal treatment (Fig. 2f and S7).[37–39] X-ray photoelectron spectroscopy (XPS) was further conducted to probe the chemical states and bonding environments (Fig. 2g and S8). Compared with pure ZIF-67 powder, the peaks of Co^{3+} and Co^{2+} in the Co 2p spectrum shift by 0.7 eV, while the Co–N bond in the N 1s spectrum shifts by −0.6 eV. These shifts confirm significant modifications in the oxidation state and electronic environment of cobalt, consistent with the transformation from Co–N coordination in ZIF-67 to Co–N bonding in 67 MC@Cu. In addition, thermal decomposition of the organic ligands induces a transformation in nitrogen coordination, specifically converting pyridinic-N into the more thermodynamically stable pyrrolic-N configuration (Fig. S8).[40]

To gain nanoscale structural insights, high-resolution transmission electron microscopy (HRTEM) was employed. Cross-sectional lamellae of 67 MC@Cu were prepared using a focused ion beam (Fig. S9). The HRTEM image reveals two distinct phase interfaces in 67 MC@Cu (Fig. 2i). Lattice-fringe analysis shows that the yellow and blue regions correspond to the Cu (200) plane ($d = 0.18$ nm, Fig. 2h) and the characteristic (111) plane of CoN ($d = 0.24$ nm, Fig. 2j), respectively. The amorphous regions correspond to the carbon skeleton formed during thermal treatment.[41–43] These findings demonstrate the successful preparation and close interfacial bonding of 67 MC on the Cu CC. Elemental TEM-EDS mapping shows homogeneous distributions of C, N, and Co throughout 67 MC@Cu

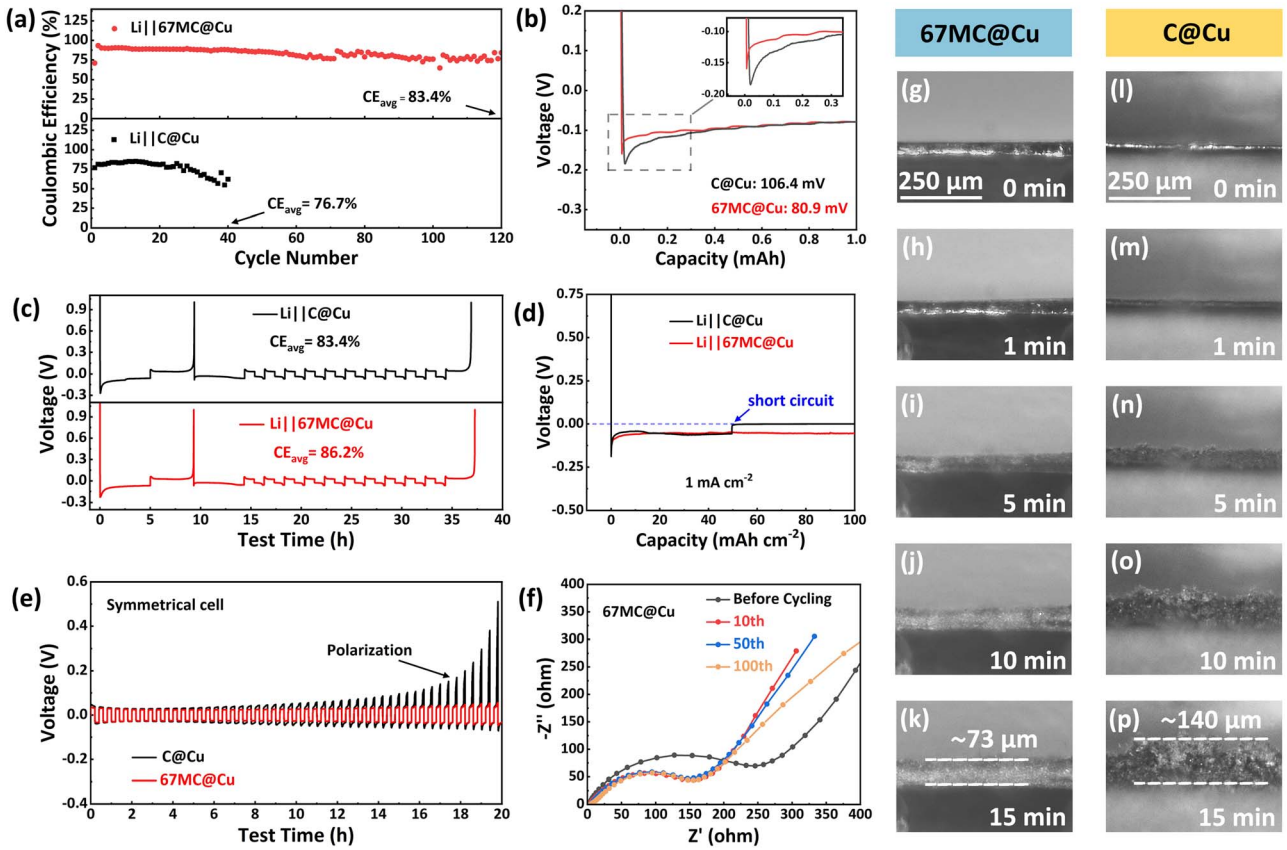

Fig. 3 (a) Comparison of CE of Li deposition and stripping processes on C@Cu and 67 MC@Cu at a current density of 1 mA cm^{-2} with a fixed capacity of 1 mA h cm^{-2}. (b) Voltage–capacity curves during initial Li$^+$ deposition on C@Cu and 67 MC@Cu at a current density of 1 mA cm^{-2}. (c) Time–voltage curves of Li||C@Cu and Li||67 MC@Cu half-cells in the Aurbach CE test. (d) Time–voltage curves of Li||C@Cu and Li||67 MC@Cu half-cells during continuous discharge at 1 mA cm^{-2}. (e) Time–voltage curves of the symmetric cells assembled with C@Cu and 67 MC@Cu (prelithiation: 5 mA h cm^{-2}). (f) Electrochemical impedance spectroscopy of the Li||67 MC@Cu half-cell at different states. *In situ* optical microscopy images of Li deposition on the (g–k) 67 MC@Cu and (l–p) C@Cu at a current density of 10 mA cm^{-2}.

(Fig. S10). Furthermore, even after immersion in the electrolyte for 12 h, the Co 2p XPS spectrum of 67 MC@Cu remains nearly unchanged compared with pristine 67 MC, confirming its high chemical stability (Fig. 2k).

Having established the structural and interfacial features, the electrochemical properties of 67 MC@Cu as an AFLMB CC were evaluated in Li||67 MC@Cu half-cells.[44] At 1 mA cm^{-2} with a fixed areal capacity of 1 mA h cm^{-2}, the Li||67 MC@Cu cell demonstrates excellent cycling stability, maintaining an average coulombic efficiency (CE$_{avg}$) of 83.4% over 120 cycles (Fig. 3a). By contrast, the Li||C@Cu cell suffers rapid capacity fading and delivers a lower CE$_{avg}$ of 76.7% within only 40 cycles. The initial Li deposition behavior was further investigated by measuring the nucleation overpotential, defined as the potential difference between the minimum voltage dip and the subsequent stable deposition plateau (Fig. 3b).[45] The overpotential is significantly lower for 67 MC@Cu (80.9 mV) compared with C@Cu (106.4 mV), indicating facilitated Li nucleation. This improvement is attributed to the synergistic effect of the conductive carbon skeleton and lithiophilic CoN species. To examine the influence of fabrication parameters, half-cells based on Cu-2h-400 and Cu-3h-350 were also tested. As shown in Fig. S11 and S12, both samples exhibit a lower CE$_{avg}$ and higher nucleation overpotential compared to 67 MC@Cu, suggesting that elevated thermal treatment temperature and excessive thickness exert a detrimental effect on Li deposition.

The reversibility of Li deposition/stripping was evaluated using the Aurbach CE test.[46–48] The activated Li||67 MC@Cu half-cell exhibits a moderate average CE$_{avg}$ of 86.2% (Fig. 3c). This value primarily arises from the use of a conventional carbonate-based electrolyte without additives, which was chosen to highlight the intrinsic effect of CC modification. In addition, the high lithiophilicity and abundant internal cavities of the 67 MC framework can lead to the formation of "self-preserved" Li seeds that facilitate homogeneous Li redeposition in subsequent cycles. Nevertheless, the CE$_{avg}$ of 67 MC@Cu still surpasses that of Li||C@Cu (83.4%), demonstrating its practical promise in AFLMBs. The time–voltage profiles of continuous Li deposition were monitored over 100 h to evaluate the limiting areal capacities at different current densities.[49] At 1 mA cm^{-2}, Li||C@Cu short-circuits at only 50 mA h cm^{-2}, whereas Li||67 MC@Cu sustains stable Li deposition up to 100 mA h cm^{-2} (Fig. 3d). Similarly, at higher current densities (Fig. S13), 67 MC@Cu maintains stable Li plating for over 100 h (300 mA h cm^{-2}) at 3 mA cm^{-2} and 40 h (200 mA h cm^{-2}) at 5

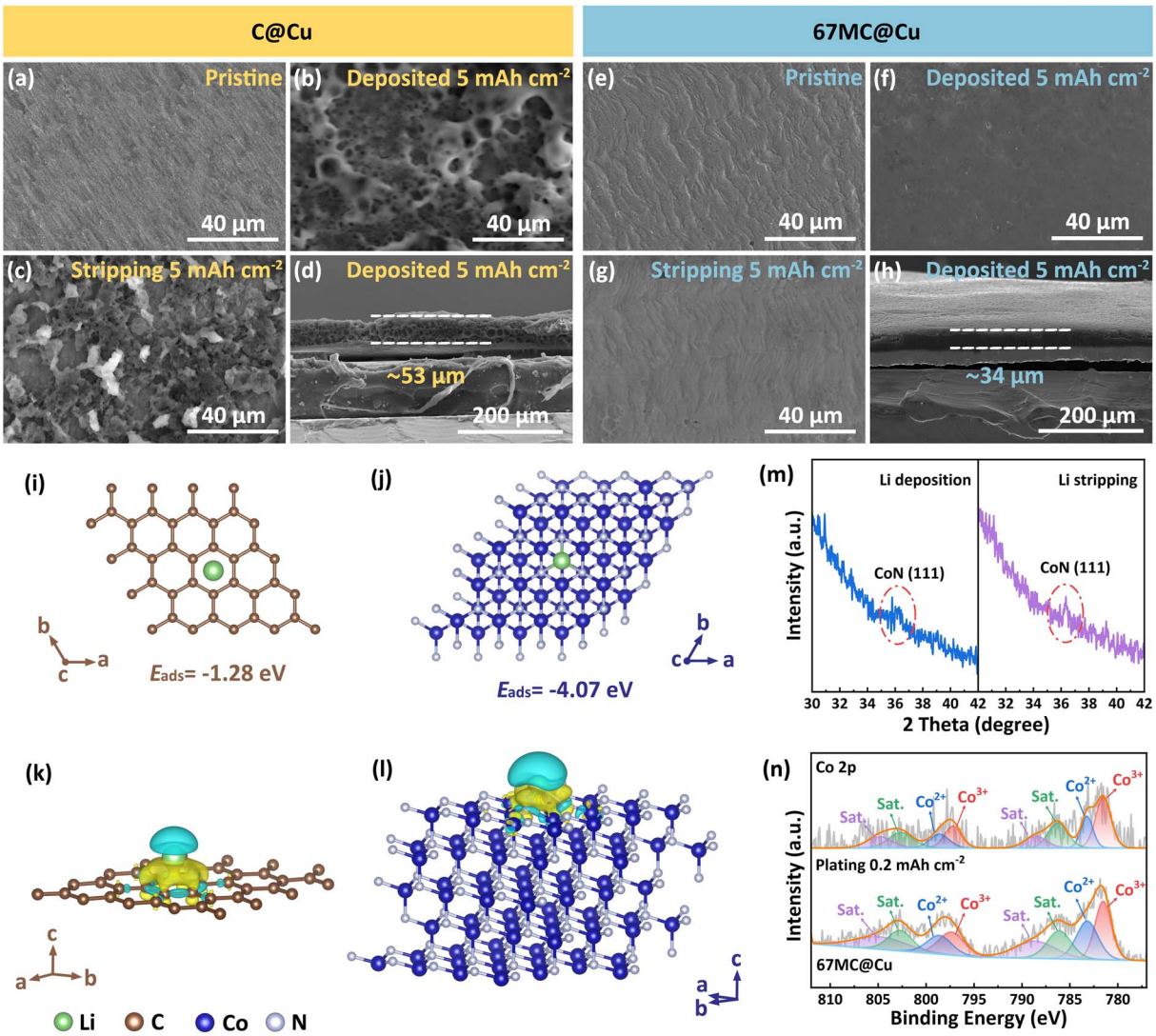

Fig. 4 SEM images of (a) pristine C@Cu CC, (b) C@Cu CC after depositing 5 mA h cm^{-2} Li, (c) C@Cu CC after stripping 5 mA h cm^{-2} Li, and (d) cross-sectional image of C@Cu CC after depositing 5 mA h cm^{-2} Li. SEM images of (e) pristine 67 MC@Cu CC, (f) 67 MC@Cu CC after depositing 5 mA h cm^{-2} Li, (g) 67 MC@Cu CC after stripping 5 mA h cm^{-2} Li, (h) cross-sectional image of 67 MC@Cu CC after depositing 5 mA h cm^{-2} Li. Li adsorption models (i) Li on Carbon and (j) Li on CoN (111). Differential charge density distributions for different Li adsorption models: (k) Li on carbon and (l) Li on CoN (111). (m) XRD patterns of 67 MC@Cu after Li deposition (0.2 mA h cm^{-2}) and stripping. (n) High-resolution Co 2p XPS spectra of 67 MC@Cu in the initial state and after Li deposition (0.2 mA h cm^{-2}).

mA cm^{-2}, respectively, far exceeding the performance of C@Cu. Moreover, 67 MC@Cu exhibits consistently lower nucleation overpotentials than C@Cu at all current densities, confirming its ability to promote rapid and uniform Li nucleation, effectively accommodate high Li flux, and suppress dendrite-induced failure.

The Li deposition process was directly visualized using an *in situ* optical microscope (Fig. 3g–p).[50,51] After 15 min of continuous Li deposition at 10 mA cm^{-2}, C@Cu develops a coarse and porous Li layer (140 μm thick) dominated by dendritic growth. In contrast, 67 MC@Cu promotes uniform and compact Li deposition with a reduced thickness of 73 μm. The results confirm that 67 MC@Cu regulates Li^+ nucleation and growth, enabling homogeneous Li deposition and mitigating dendrite-induced short-circuit risks. The interfacial stability was further evaluated *via* electrochemical impedance spectroscopy (EIS).[52,53] In Li||C@Cu cells, interfacial resistance increases markedly with cycling (Fig. S14), whereas 67 MC@Cu maintains stable impedance values (Fig. 3f, S15 and S16). Finally, symmetric cells were assembled after prelithiation of C@Cu and 67 MC@Cu CCs (Fig. 3e). At 1 mA cm^{-2} and 0.2 mA h cm^{-2} per cycle, the C@Cu-based symmetric cell shows rapidly increased polarization within 12 h, while the 67 MC@Cu-based cell retains stable voltage profiles. Together, these results demonstrate that 67 MC@Cu not only facilitates uniform Li deposition but also effectively enhances electrode–electrolyte interfacial stability during long-term cycling.

The morphologies of the 67 MC@Cu and C@Cu CCs under different Li deposition/stripping states (current density: 1 mA cm^{-2}) were examined using SEM.[54] For C@Cu, Li dendrites

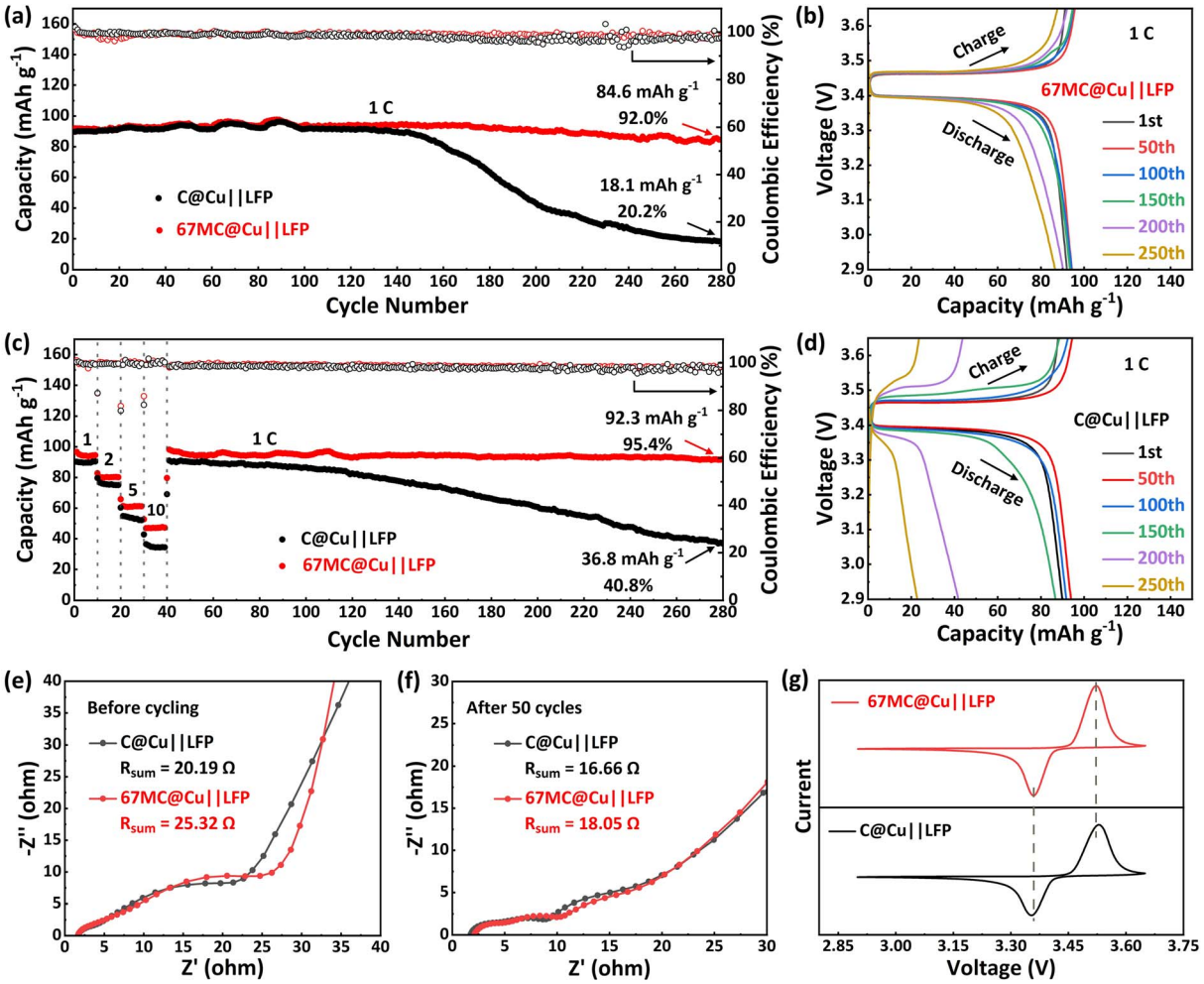

Fig. 5 (a) Cycling performance of C@Cu||LFP and 67 MC@Cu||LFP at 1C (1C = 170 mA h g^{-1}). (prelithiation: 5 mA h cm^{-2}; activation: 0.2C, 2 cycles). Charge and discharge curves at different cycles of (b) 67 MC@Cu||LFP and (d) C@Cu||LFP. (c) Rate performance comparison between C@Cu||LFP and 67 MC@Cu||LFP. EIS spectra of C@Cu||LFP and 67 MC@Cu||LFP (e) before cycling and (f) after 50 cycles. (g) CV curves of C@Cu||LFP and 67 MC@Cu||LFP (scan rate: 1 mV s^{-1}).

emerge even at a low deposition capacity of 0.5 mA h cm^{-2} (Fig. S17a) and develop into a loose, porous Li layer with increasing deposition (Fig. 4b, S17b and c). Moreover, significant Li residues remain after stripping, leading to a decline in CE (Fig. 4c). In sharp contrast, 67 MC@Cu maintains a smooth surface throughout deposition, enabling the formation of a uniform and compact Li layer (Fig. 4f and S18a–c). After stripping, the surface of 67 MC@Cu is nearly restored to its pristine morphology without detectable residues (Fig. 4g). Cross-sectional SEM further highlights these differences. At a deposition capacity of 5 mA h cm^{-2}, 67 MC@Cu yields a dense Li layer with a thickness of 34 μm (Fig. 4h and S18d), whereas C@Cu generates a loose and porous structure of 53 μm (Fig. 4d and S17d). These results demonstrate that 67 MC@Cu substantially improves the reversibility of Li deposition/stripping. The high-density Li layer also helps mitigate AFLMB volume fluctuations during cycling, thereby extending cell lifespan.

The underlying mechanism of performance enhancement was elucidated by density functional theory (DFT) calculations.[55–57] Fig. 4i shows the adsorption model of the carbon layer in C@Cu. Because of its symmetric electron distribution, Li^+ preferentially adsorbs at the hexagonal center with an adsorption energy (E_{ads}) of −1.28 eV. In contrast, for the CoN model, Li^+ adsorption occurs near the N atom, forming a stable Li–N bond with the lone pair electrons of N. This results in a markedly lower E_{ads} of −4.07 eV (Fig. 4j). The electronic structures following lithium-ion adsorption were elucidated through a differential charge-density analysis (Fig. 4k and l). The Li-CoN system exhibits a more delocalized charge distribution. This redistribution originates from the intrinsically lower work function of CoN compared with carbon, which facilitates electron transfer to Li^+ and induces an interfacial dipole that homogenizes the local electric field.[58,59] Meanwhile, the conductive carbon skeleton promotes additional charge delocalization, resulting in a more uniform interfacial charge distribution across the Li-CoN interface and thereby enabling

uniform Li nucleation.[60] Therefore, CoN serves a dual electronic role within the 67 MC@Cu CC: CoN as lithiophilic nucleation sites that lower the energy barrier for Li deposition and ensuring efficient charge transport and dendrite-free Li growth.

To evaluate the stability of CoN, *ex situ* XRD and XPS analyses were performed after depositing 0.2 mA h cm^{-2} of Li (Fig. 4m and n). The XRD patterns show that the (111) peak of CoN remains clearly identifiable, while XPS analysis confirms that the valence of Co atoms is essentially unchanged, indicating that CoN retains its structural integrity during the Li deposition process. To further assess the long-term stability of CoN, additional *ex situ* XRD and XPS measurements were conducted on Li‖67 MC@Cu half-cells after 100 cycles (Fig. S19). The XRD patterns still display the characteristic CoN peaks, and Co 2p XPS spectra after Ar^+ etching show Co^{2+}/Co^{3+} peaks, confirming that the CoN remains unchanged after cycling. These results demonstrate that CoN maintains excellent stability both during initial Li deposition and long-term cycling, ensuring durable interfacial regulation of Li plating and stripping.

The practical applicability of 67 MC@Cu was evaluated in full cells paired with a $LiFePO_4$ (LFP) cathode. As shown in Fig. 5a and b, 67 MC@Cu‖LFP demonstrates excellent long-term cycling stability, retaining 84.6 mA h g^{-1} with 92% capacity retention after 280 cycles. In comparison, C@Cu‖LFP exhibits severe degradation, retaining only 18.1 mA h g^{-1} under identical conditions (Fig. 5d). A comprehensive comparison with previously reported studies (Table S1) further confirms the advanced performance of 67 MC@Cu CC over other modified Cu CC. This enhanced performance is further demonstrated in rate capability tests (Fig. 5c and S20). With current density increasing from 1C to 10C, 67 MC@Cu‖LFP experiences less capacity loss than C@Cu‖LFP. When the current density is returned to 1C after 40 cycles, 67 MC@Cu‖LFP also shows higher capacity and stronger cyclic stability than C@Cu‖LFP (95.4% *vs.* 40.8% retention after 280 cycles).

EIS analysis reveals that the initial resistance of 67 MC@Cu‖LFP is slightly higher than that of C@Cu‖LFP, attributed to the presence of the 67 MC layer (Fig. 5e). After 50 cycles, the impedance of both cells reaches a similar level (16.66 Ω for C@Cu‖LFP and 18.05 Ω for 67 MC@Cu‖LFP) (Fig. 5f and S21). Furthermore, cyclic voltammetry curves (2.9–3.65 V) show that 67 MC@Cu‖LFP possesses a narrower redox peak separation than C@Cu‖LFP (Fig. 5g), indicating faster charge-transfer kinetics and more reversible redox processes.[61]

Considering the strong electrolyte dependence of AFLMB stability, the electrochemical behavior of 67 MC@Cu was tested in different electrolytes. In the localized high-concentration electrolyte (LHCE, 2.4F-1.6N-TTE), the Li‖67 MC@Cu half-cell exhibits a stable CE of 98.0% for 130 cycles (Fig. S22a), and the prelithiated 67 MC@Cu‖LFP full cell maintains stable cycling for 500 cycles at 5C (Fig. S22b). In the ether-based electrolyte, the Li‖67 MC@Cu half-cell achieves a stable CE of 91.5% over 60 cycles (Fig. S22c), while the corresponding prelithiated 67 MC@Cu‖LFP full cell delivers stable operation for 160 cycles at 5C (Fig. S22d). These results confirm that 67 MC@Cu delivers outstanding electrochemical performance and strong practical potential.

3. Conclusions

This work reports a CoN-doped carbon skeleton-modified Cu CC (67 MC@Cu), prepared *via in situ* liquid-phase epitaxial growth of a ZIF-67 polycrystalline membrane followed by thermal treatment. The formation and lithiophilicity of CoN were validated through HRTEM and DFT calculations. *In situ* optical microscopy and SEM observations further confirmed that 67 MC@Cu enables homogeneous lithium nucleation and promotes the formation of a compact, high-density Li deposition layer. As a result, Li‖67 MC@Cu half-cells exhibit superior deposition/stripping reversibility, while full cells paired with an LFP cathode deliver remarkable long-term cycling stability, retaining 92% of their capacity after 280 cycles, significantly exceeding the 20.2% retention of commercial C@Cu. The 67 MC@Cu CC also demonstrates good adaptability across different electrolytes. Overall, this work demonstrates a binder-free, MOF-derived modification strategy that effectively overcomes the limitations of conventional CCs, offering a promising pathway toward practical implementation of AFLMBs and providing new insights into interfacial engineering design.

Author contributions

Wenyu Ma: design and execution of the experiments and preparation of the article draft. Haiyang Wu: design of experiments, writing – reviewing and editing. Lingtong Zhu: validation, data curation, writing – reviewing and editing. Zhenming Xu: theoretical calculations. Bing Ding: validation, data curation. Hui Dou: writing – reviewing and editing, supervision. Xiaogang Zhang: supervision, project administration, funding acquisition, writing – reviewing and editing.

Conflicts of interest

There are no conflicts to declare.

Data availability

The data supporting this article have been included as part of the supporting information (SI). Supplementary information: experimental procedures, supplementary characterizations (SEM, AFM, XRD, XPS analyses) and electrochemical testing. See DOI: **https://doi.org/10.1039/d5sc06967j**.

Acknowledgements

This work was supported by the National Key Research and Development Project Intergovernmental International Science and Technology Innovation Cooperation (2022YFE0109400), Leading Edge Technology of Jiangsu Province (BK20232022 and BK20220009), and the High Performance Computing Platform of Nanjing University of Aeronautics and Astronautics. We acknowledge the Center for Microscopy and Analysis at the Nanjing University of Aeronautics and Astronautics for advanced facilities. We thank Scientific Compass (**https://www.shiyanjia.com**) for the XPS analysis and language revision.

References

1 Z. Huang, H. Lyu, L. C. Greenburg, Y. Cui and Z. Bao, *Nat. Energy*, 2025, **10**, 811–823.
2 T. Wang, B. Chen, Y. Liu, Z. Song, Z. Wang, Y. Chen, Q. Yu, J. Wen, Y. Dai, Q. Kang, F. Pei, R. Xu, W. Luo and Y. Huang, *Science*, 2025, **388**, 311–316.
3 W. Yang, A. Chen, P. He and H. Zhou, *Nat. Commun.*, 2025, **16**, 4229.
4 K. Ryu, K. Lee, J. Lim, M. J. Lee, K. Kim, U. H. Lee, B. L. D. Rinkel, K. Kim, S. Kim, D. Kim, D. Shin, B. McCloskey, J. Kang and S. W. Lee, *Energy Environ. Sci.*, 2024, **17**, 7772–7781.
5 C. Zhang, Y. Guo, S. Tan, Y. Wang, J. Guo, Y. Tian, X. - Zhang, B. Liu, S. Xin, J. Zhang, L. Wan and Y. Guo, *Sci. Adv.*, 2024, **10**, eadl4842.
6 X. Li, Y. Bai, J. Jing, T. Ren, Z. Wang, J. Ma and K. Sun, *Adv. Funct. Mater.*, 2025, **35**, 2421329.
7 F. Xu, Y. Wu, L. Wang, Z. Zhang, G. Liu, C. Guo, D. Wu, C. Yi, J. Luo, W. He, C. Xu, M. Yang, H. Li, L. Chen and F. Wu, *Adv. Energy Mater.*, 2025, **15**, 2405369.
8 S. Kim, G. Park, S. J. Lee, S. Seo, K. Ryu, C. H. Kim and J. W. Choi, *Adv. Mater.*, 2023, **35**, 2206625.
9 S. Chen, C. Pan, Q. Wang, J. Luo and X. Fu, *Adv. Funct. Mater.*, 2024, **34**, 2409812.
10 J. Wang, J. Luo, H. Wu, X. Yu, X. Wu, Z. Li, H. Luo, H. Zhang, Y. Hong, Y. Zou, S. Cao, Y. Qiao and S. Sun, *Angew. Chem., Int. Ed.*, 2024, **63**, e202400254.
11 S. E. Sandoval, C. G. Haslam, B. S. Vishnugopi, D. W. Liao, J. S. Yoon, S. H. Park, Y. Wang, D. Mitlin, K. B. Hatzell, D. J. Siegel, P. P. Mukherjee, N. P. Dasgupta, J. Sakamoto and M. T. McDowell, *Nat. Mater.*, 2025, **24**, 673–681.
12 X. Duan, J. Sun, L. Shi, S. Dong and G. Cui, *Interdiscip. Mater.*, 2025, **4**, 217–234.
13 Y. An, Y. Zeng, D. Luan and X. Lou, *Matter*, 2024, **7**, 1466–1502.
14 L. Lin, H. Zheng, Q. Luo, J. Lin, L. Wang, Q. Xie, D. Peng and J. Lu, *Adv. Funct. Mater.*, 2024, **34**, 2315201.
15 G. Lai, J. Jiao, C. Fang, Y. Jiang, L. Sheng, B. Xu, C. Ouyang and J. Zheng, *Small*, 2023, **19**, 2205416.
16 N. Li, J. Zhao, Y. Zhang, R. Song, N. Zhang, Y. Cui, J. Lin, H. Xu and Y. Huang, *Adv. Funct. Mater.*, 2025, **35**, 2419102.
17 Z. Hao, Y. Lu, G. Yang, Q. Zhao, Z. Yan and J. Chen, *Adv. Mater.*, 2025, **37**, 2415258.
18 X. Zhang, L. Ma, Y. Cai, J. Fransaer and Q. Zheng, *Matter*, 2024, **7**, 583–602.
19 H. Kwon, J.-H. Lee, Y. Roh, J. Baek, D. J. Shin, J. K. Yoon, H. J. Ha, J. Y. Kim and H.-T. Kim, *Nat. Commun.*, 2021, **12**, 5537.
20 G. Li, D. Dong, D. Bedrov, Q. Cai, H. Wu, Z. Wang, J. Liu, K. Xu, L. Xing and W. Li, *Joule*, 2025, **9**, 101874.
21 S. K. Park, D. Copic, T. Z. Zhao, A. Rutkowska, B. Wen, K. Sanders, R. He, H.-K. Kim and M. De Volder, *ACS Nano*, 2023, **17**, 14658–14666.
22 X. Gao, P. Du, B. Cheng, X. Ren, X. Zhan and L. Zhu, *ACS Appl. Mater. Interfaces*, 2024, **16**, 7327–7337.
23 Y. Tian, Z. Pei, D. Luan and X. Lou, *Angew. Chem., Int. Ed.*, 2025, **137**, e202423454.
24 Q. Zhang, X. Gu, B. Li, Q. Chen, Q. Zhai, C. Jin, Y. Jiao, W. Yang, J. Zuo, P. Kang, Z. Zhao, X. Zhang, P. Zhai and Y. Gong, *Adv. Funct. Mater.*, 2025, 2508957.
25 B. Wang, W. Li, J. Liu, T. Gan, S. Gao, L. Li, T. Zhang, Y. Zhou, Z. Shi, J. Li, Y. Liu and J. Yu, *Adv. Mater.*, 2025, **37**, 2407154.
26 O. M. Yaghi, G. Li and H. Li, *Nature*, 1995, **378**, 703–706.
27 N. Sun, S. S. A. Shah, Z. Lin, Y. Zheng, L. Jiao and H. Jiang, *Chem. Rev.*, 2025, **125**, 2703–2792.
28 L. Chai, R. Li, Y. Sun, K. Zhou and J. Pan, *Adv. Mater.*, 2025, **37**, 2413658.
29 X. Zhao, K. Tao and L. Han, *Nanoscale*, 2022, **14**, 2155–2166.
30 J. Li, X. Jing, S. Li, L. Ma, Y. Yang, S. Han, J. Jia, C. T. Yavuz and G. Zhu, *Matter*, 2025, **8**, 102047.
31 T. Zhao, S. Li, F. Liu, Z. Wang, H. Wang, Y. Liu, X. Tang, M. Bai, M. Zhang and Y. Ma, *Energy Storage Mater.*, 2022, **45**, 796–804.
32 C. Song, Z. Li, L. Ma, M. Li, S. Huang, X. Hong, Y. Cai and Y. Lan, *ACS Nano*, 2021, **15**, 13436–13443.
33 H. Wu, L. Wu, Y. Li, W. Dong, W. Ma, S. Li, D. Xiao, P. Huang and X. Zhang, *Angew. Chem., Int. Ed.*, 2025, **64**, e202417209.
34 H. Wang, Y. Mao, P. Xu, Y. Ding, H. Yang, J. F. Li, Y. Gu, J. Han, L. Zhang and B.-W. Mao, *Energy Environ. Sci.*, 2025, **18**, 2622–2633.
35 H. Chen, A. Hou, C. Zheng, J. Tang, K. Xie and A. Gao, *ACS Appl. Mater. Interfaces*, 2020, **12**, 24505–24511.
36 C. Duan, Z. Cheng, B. Wang, J. Zeng, J. Xu, J. Li, W. Gao and K. Chen, *Small*, 2021, **17**, 2007306.
37 H. Hong, J. Liu, H. Huang, C. Atangana Etogo, X. Yang, B. Guan and L. Zhang, *J. Am. Chem. Soc.*, 2019, **141**, 14764–14771.
38 W. Zhang, C. Li, J. Ji, Z. Niu, H. Gu, B. F. Abrahams and J. Lang, *Chem. Eng. J.*, 2023, **461**, 141937.
39 S. Qiu, H. Shao, C. He, X. Song, J. Fan, Y. Xue, G. Li and S. Xiao, *App. Catal. B: Environ.*, 2024, **344**, 123615.
40 R. Zhu, J. Ding, J. Yang, H. Pang, Q. Xu, D. Zhang and P. Braunstein, *ACS Appl. Mater. Interfaces*, 2020, **12**, 25037–25041.
41 L. Wang, W. He, D. Yin, H. Zhang, D. Liu, Y. Yang, W. Yu and X. Dong, *Renew. Sust. Energ. Rev.*, 2023, **181**, 113354.
42 Y. Tang, J. Ding, W. Zhou, S. Cao, F. Yang, Y. Sun, S. Zhang, H. Xue and H. Pang, *Adv. Sci.*, 2023, **10**, 2206960.
43 F. Wang, J. Gao, Y. Liu and F. Ren, *J. Mater. Chem. A*, 2022, **10**, 17395–17405.
44 E. Kim, M. An, C. Lee, H. An and Y. Son, *ACS Appl. Energy Mater.*, 2025, **8**, 6746–6755.
45 X. Li, Y. Su, Y. Qin, F. Huang, S. Mei, Y. He, C. Peng, L. Ding, Y. Zhang, Y. Peng and Z. Deng, *Adv. Mater.*, 2023, **35**, 2303489.
46 D. Aurbach, O. Youngman and P. Dan, *Electrochim. Acta*, 1990, **35**, 639–655.
47 A. Mohammadi, S. Djafer, S. Sayegh, A. J. Naylor, M. Bechelany, R. Younesi, L. Monconduit and L. Stievano, *Chem. Mater.*, 2023, **35**, 2381–2393.

48 R. Li, X. Huang, H. Zhang, J. Wang, Y. Fan, Y. Huang, J. Liu, M. Yang, Y. Yu, X. Xiao, Y. Tan, H. B. Wu, L. Fan, T. Deng, L. Chen, Y. Shen and X. Fan, *Nat. Commun.*, 2025, **16**, 4672.
49 Y. Lu, C. Zhao, H. Yuan, X. Cheng, J. Huang and Q. Zhang, *Adv. Funct. Mater.*, 2021, **31**, 2009925.
50 L. Lin, K. Qin, Y. Hu, H. Li, X. Huang, L. Suo and L. Chen, *Adv. Mater.*, 2022, **34**, 2110323.
51 H. Wu, W. Ma, L. Wu, W. Dong, Y. Li, Z. Fan, X. Zhao, P. Huang and X. Zhang, *Angew. Chem., Int. Ed.*, 2025, e202506222.
52 J. Li, L. Shen, Z. Cheng, J. Zhang, L. Li, Y. Zhang, Y. Gao, C. Guo, X. Chen, C. Zhao, R. Zhang and Q. Zhang, *J. Energy Chem.*, 2025, **101**, 16–22.
53 L. Xu, Y. Xiao, Z. Yu, Y. Yang, C. Yan and J. Huang, *Angew. Chem., Int. Ed.*, 2024, **63**, e202406054.
54 P. Zou, C. Wang, J. Qin, R. Zhang and H. L. Xin, *Energy Storage Mater.*, 2023, **58**, 176–183.
55 H. Wang, L. Zhao, H. Zhang, Y. Liu, L. Yang, F. Li, W. Liu, X. Dong, X. Li, Z. Li, X. Qi, L. Wu, Y. Xu, Y. Wang, K. Wang, H. Yang, Q. Li, S. Yan, X. Zhang, F. Li and H. Li, *Energy Environ. Sci.*, 2022, **15**, 311–319.
56 Z. Xu and H. Zhu, *J. Phys. Chem. C*, 2018, **122**, 14918–14927.
57 W. Meng, Z. Dang, D. Li, L. Jiang and D. Fang, *Adv. Funct. Mater.*, 2022, **32**, 2204364.
58 R. Zeng, H. Li, Z. Shi, L. Xu, J. Meng, W. Xu, H. Wang, Q. Li, C. J. Pollock, T. Lian, M. Mavrikakis, D. A. Muller and H. D. Abruna, *Nat. Mater.*, 2024, **23**, 1695–1703.
59 X. Chen, X. Chen, T. Hou, B. Li, X. Cheng, R. Zhang and Q. Zhang, *Sci. Adv.*, 2019, **5**, eaau7728.
60 Y. Yang, R. Zeng, Y. Xiong, F. J. DiSalvo and H. D. Abruna, *J. Am. Chem. Soc.*, 2019, **141**, 19241–19245.
61 F. Wan, L. Zhang, X. Dai, X. Wang, Z. Niu and J. Chen, *Nat. Commun.*, 2018, **9**, 1656.